Nano Research

Open Access

Research Article

Dynamic evolution of Co species and morphological reconstruction on Co-N-C during the nitrate reduction reaction in neutral solution

Yuanlin Fu[1], Xiaoting Yang[2], Ya Yu[2], Kang Zhou[3], Xiaoyang Ye[1], Aoxiang Zhang[1], Xiaojiao Hou[1], Bingbing Chen[1], Fuqiang Fan[1], Yuhang Li[1], and Yu Fu[1] ✉

[1] *Department of Chemistry, College of Sciences, Northeastern University, Shenyang 110819, China*
[2] *Department of Physical Education, Shen Yang Institute of Science and Technology, Shenyang 110167, China*
[3] *Sungrow Power Supply Co., Ltd., Hefei 230088, China*

Cite this article: *Nano Research*, **2025**, *18*, 94907038. https://doi.org/10.26599/NR.2025.94907038

ABSTRACT: The electrochemical nitrate reduction reaction (eNO_3^-RR) is considered an effective approach for converting nitrate-containing wastewater to ammonia. The adsorption and activation of NO_3^- is the critical step for many materials and the high energy barrier inhibits the continuation of the reduction reaction. The Co nanoparticles encapsulated in the carbon layer we prepared spontaneously react with NO_3^- and the resulting Co^{2+} is then reduced by electroreduction to Co^0, which circulates continuously. This resulted in overcoming the energy input required for NO_3^- adsorption and conversion, thereby increasing the catalytic activity. At the same time, the morphology of the catalyst reconstructed from a dodecahedron to an interwoven nanosheet structure and the increased surface area also gives it better properties. The obtained $Co(OH)_2$@Co-N-C has an excellent eNO_3^-RR of 2774.7 $\mu g \cdot h^{-1} \cdot cm^{-2}$ with a Faraday efficiency of 81.4% in neutral solution. At the same time, the material-modified electrode can run stably for more than 100 h. Our work provides a new idea for the design of Co-based catalysts for eNO_3^-RR.

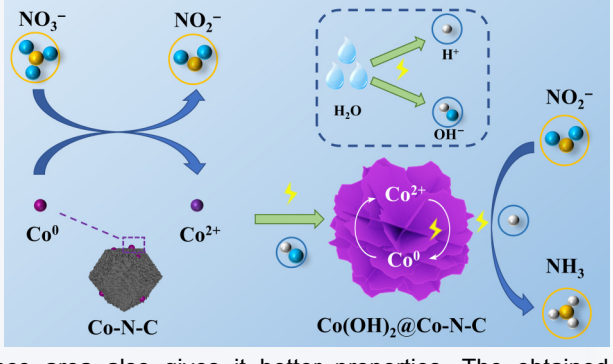

KEYWORDS: electrochemical nitrate reduction reaction, Co-based catalyst, dynamic evolution of Co species, morphological reconstruction

1 Introduction

Nitrates (NO_3^-) are widespread in surface waters due to factory emissions and the use of pesticides and fertilizers [1]. It can lead to water quality degradation, soil contamination and even risks to human health [2, 3]. How to efficiently convert NO_3^- in wastewater into nitrogen-containing additives is very important. At present, membrane separation [4], ion exchange [5] and chemical reduction [6] methods have been used to eliminate NO_3^- in the solution. The electrocatalytic nitrate reduction reaction requires mild conditions, simple equipment and can convert the NO_3^- to ammonia, so it has been studied extensively in recent years [7–10]. As we know, electrochemical nitrate reduction reaction (eNO_3^-RR) involves a complex eight-electron, nine-proton transfer process ($NO_3^- + 8e^- + 9H^+ \rightarrow NH_3 + 3H_2O$), so how to design an efficient catalyst that is suitable for the reduction reaction is crucial.

Transition metal-based catalysts with different nanostructures and compositions, such as Cu, Fe and Ni-based single atom or compound catalysts, are considered promising choices due to their abundance and low cost [11–20]. Among them, Co-based catalysts exhibit high catalytic activity for the reduction of NO_3^- due to their unique electronic structure and structural adjustability. For example, CoO_x nanosheets rich in adsorbed oxygen have been reported [21]. The excessive oxygen on the cobalt oxide surface suppresses the competition hydrogen evolution reaction (HER) by enhancing the interaction with *H. In addition, one kind of Co-based metal-organic framework (Co-terephthalic acid (Co-TPA)) has been fabricated for eNO_3^-RR [22]. Co-TPA *in-situ* changes into the CoOOH phase in the process of the reaction can be seen as the real active sites. By incorporating the highly electronegative Cu ions into the Co-TPA, the electron cloud distribution at the Co active sites was adjusted. The adsorption of NO_3^- was improved and a good NH_3 yield of 1.12 $mmol \cdot h^{-1} \cdot cm^{-2}$ in strongly basic solutions

Received: August 4, 2024; **Revised:** August 31, 2024
Accepted: September 18, 2024

✉Address correspondence to fuyu@mail.neu.edu.cn

was obtained. Furthermore, a series of Ru_xCo_y hollow nano dodecahedrons [23] were used in NO_3^-RR, finding optimal performance by controlling the ratio of the two metals. Liang et al. [24] reported a kind of Mn-doped $Co(OH)_2$. Mn plays a key role in inhibiting H* binding, thereby ensuring a much higher Faraday efficiency (FE) for ammonia production. However, the simultaneous explanation of morphological changes and dynamic evolution of valence states of Co-based catalysts during the eNO_3^-RR has rarely been reported.

In this work, we have successfully prepared an N-doped carbon-encapsulated Co nanoparticle (Co-N-C) derived from zeolitic imidazolate framework-67 (ZIF-67). The Co^0 in Co-N-C spontaneously reacts with NO_3^- in solution to generate Co^{2+} and NO_2^- and then Co^{2+} combines with OH^- from electrolytic water to form $Co(OH)_2$. In addition, the decahedral shape of Co-N-C is reconstructed into an interwoven nanosheet structure, which we define as $Co(OH)_2$@Co-N-C. Under the reducing action of electrons, Co^{2+} is reduced to Co^0 leading to the dynamic evolution of a Co species. The spontaneous reaction avoids the energy input from the adsorption and activation processes with high energy barriers [23].

In-situ Raman spectroscopy and corresponding designed experiments also confirmed this result. Moreover, the change in morphology gives the material a larger specific surface area and the consumption of OH^- accelerates the dissociation of water, producing more reactive H^* species, which is more conducive to the subsequent protonation step. The *in-situ* dynamically derived $Co(OH)_2$@Co-N-C has an excellent eNO_3^-RR performance of 2774.7 $\mu g \cdot h^{-1} \cdot cm^{-2}$ with an FE of 81.4% at −1 V (vs. reversible hydrogen electrode (RHE)) in neutral solution. The morphology change and Co species dynamic evolution of our catalyst have been fully revealed, our work will provide insight into the design and synthesis of the Co-based eNO_3^-RR catalyst.

2 Experimental section

2.1 Materials

Sodium sulfate (Na_2SO_4, ≥ 99.7%), sodium nitrate ($NaNO_3$, ≥ 99.7%), sodium nitrite ($NaNO_2$, ≥ 99.7%), sodium nitrate-^{15}N ($Na^{15}NO_3$, ≥ 99.5%), cobalt nitrate ($Co(NO_3^-)_2$, ≥ 99%), ammonia sulfate-^{15}N ($(^{15}NH_4)_2SO_4$, ≥ 99.5%), deuterium oxide (D_2O, 99.9 atom % D), ammonia chloride (NH_4Cl, ≥ 99.8%), potassium sodium tartrate tetrahydrate ($KNaC_4H_{12}O_{10}{\cdot}4H_2O$, ≥ 99%), potash iodide (KI, ≥ 98%), maleic acid ($C_4H_4O_4$, ≥ 99%), potassium hydroxide (KOH, ≥ 99%), were purchased from Sinopharm Chemical Reagent Co. Ltd. 2-Methyl-imidazol (2-MI, ≥ 99%) were purchased from Energy Chemical Co., Ltd (Shanghai, China). Dimethyl formamide (DMF, ≥ 99.5%) and ethanol (≥ 99.7%) were purchased from Fuyu Fine Chemical Co., Ltd (Tianjin, China).

2.2 Characterizations and apparatus

The morphology and size of ZIF-67, Co-N-C and $Co(OH)_2$@Co-N-C were characterized by field-emission scanning electron microscopy (FESEM, Hitachi SU8010). Transmission electron microscopy (TEM) images and high-resolution TEM (HRTEM) images were acquired with JEOL JEM-2100F. The crystalline structures of the samples were determined using powder X-ray diffraction (PXRD, Panalytical, Empyrean) equipped with a Cu Kα radiation (K = 1.54056 Å). X-ray photoelectron spectroscopy (XPS) was tested on a Thermo Scientific SCALAB 250Xi. The isotope labeling experiments were measured by proton nuclear magnetic resonance (^{1}H NMR) measurement (Bruker 400-MHz system). Ultraviolet–visible (UV–vis) absorption spectra were measured at room temperature with a Lambda 650S. (PerkinElmer Corp, USA).

2.3 Synthesis of ZIF-67

ZIF-67 was prepared according to the previously reported method with modifications. 0.582 g $Co(NO_3)_2{\cdot}6H_2O$ and 0.57 g 2-methylimidazole were dissolved in 20 mL methanol, respectively. The above two solutions were mixed in a 250 mL Erlenmeyer flask and aged for 24 h. The purple powders were collected by centrifugation and dried in a vacuum oven for 10 h.

2.4 Synthesis of Co-N-C

The obtained ZIF-67 powders were placed in a porcelain boat and annealed for 3 h at 800 °C with a heating temperature rate of 3 $°C \cdot min^{-1}$ under nitrogen protection and the collected black powder is Co-N-C.

2.5 Preparation of Co-N-C modified carbon paper (CP)

2 mg Co-N-C powders were dispersed in 1 mL ethanol and ultrasound evenly for 10 min. The working electrode was constructed by dropping the above catalyst sprayed onto a carbon paper with an area of 1.0 cm × 1.0 cm and then dried in a vacuum drying oven for 2 h.

2.6 Electrochemical measurements

The electrochemical performance was investigated by using linear sweep voltammetry (LSV) and chronoamperometry with a CHI660E Electrochemical Station (Shanghai Chenhua Instrument Co., Ltd.). Unless the concentration is indicated, the electrolyte is 70 mL of deionized water mixed with 0.05 M Na_2SO_4 and 0.05 M $NaNO_3$ in H-cell. The CP-supported (1 cm × 1 cm), Ag/AgCl (3 M KCl) and Pt plate (1 cm × 1 cm) were used as the working electrode, the reference electrode and the counter electrode. The chronoamperometry (current–time (*i*–*t*)) measurement was conducted by different potentials for 2 h with stirring of 300 rpm. LSV tests were performed at the rate of 5 $mV \cdot s^{-1}$. The measured potentials versus Ag/AgCl were converted to the RHE scale.

3 Results and discussion

The synthesis process of imidazolone metal-organic frameworks (ZIF-67) and its derivative are illustrated in Scheme 1. ZIF-67 was prepared by the reported bottle-around-a-ship method at room temperature. Then, the powders were annealed at 800 °C under

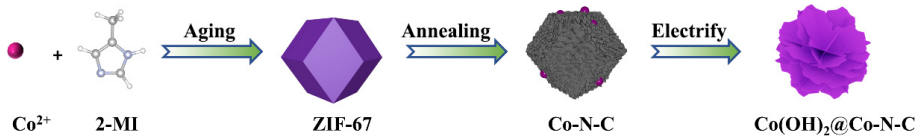

Scheme 1 Schematic illustration of the synthesis of the ZIF-67, Co-N-C and $Co(OH)_2$@Co-N-C.

nitrogen protection to obtain the derivative Co nanoparticles-nitrogen-doped carbon material (Co-N-C).

The structure and morphology of ZIF-67 were characterized first. Figures S2(a) and S2(b) in the Electronic Supplementary Material (ESM) display the SEM images of ZIF-67 and we can observe that ZIF-67 remains a smooth dodecahedron shape with a diameter that varies from 600 to 900 nm. Figure S2(c) in the ESM shows the XRD patterns of ZIF-67 and ZIF-67 simulations. For the ZIF-67 sample, all of the diffraction peaks correspond to the simulation map individually which proves the successful preparation of ZIF-67.

The morphology of the Co-N-C was investigated by SEM and TEM measurements. In contrast to the smooth surface of ZIF-67, Co-N-C has a surface that is full of particles (Fig. 1(a)). More Co^0 nanoparticles encapsulated in carbon layers can be detected in the TEM image of the catalyst (Fig. 1(b)). Meanwhile, we can observe that the elemental mapping images of O, N and Co are evenly distributed throughout the regular dodecahedron. XRD pattern was used to study the phase structure of the as-prepared sample. There are three significant diffraction peaks at 44.2°, 51.5° and 75.9°, corresponding to (111), (200) and (220) lattice planes of metal Co [25] (JCPDS No. 15-0806) (Fig. 1(c)). The chemical composition of the Co-N-C was examined by XPS measurements. The high-resolution spectra of elements of N, O and Co are shown in Figs. 1(d)–1(f). For N 1s in Fig. 1(d), the two separate peaks located at 398.97 and 400.78 eV can be assigned to pyridine-N [26] and graphitic-N [27]. There are two separate peaks in the O 1s core-line spectra, the peaks located at 529.93 and 531.65 eV correspond to

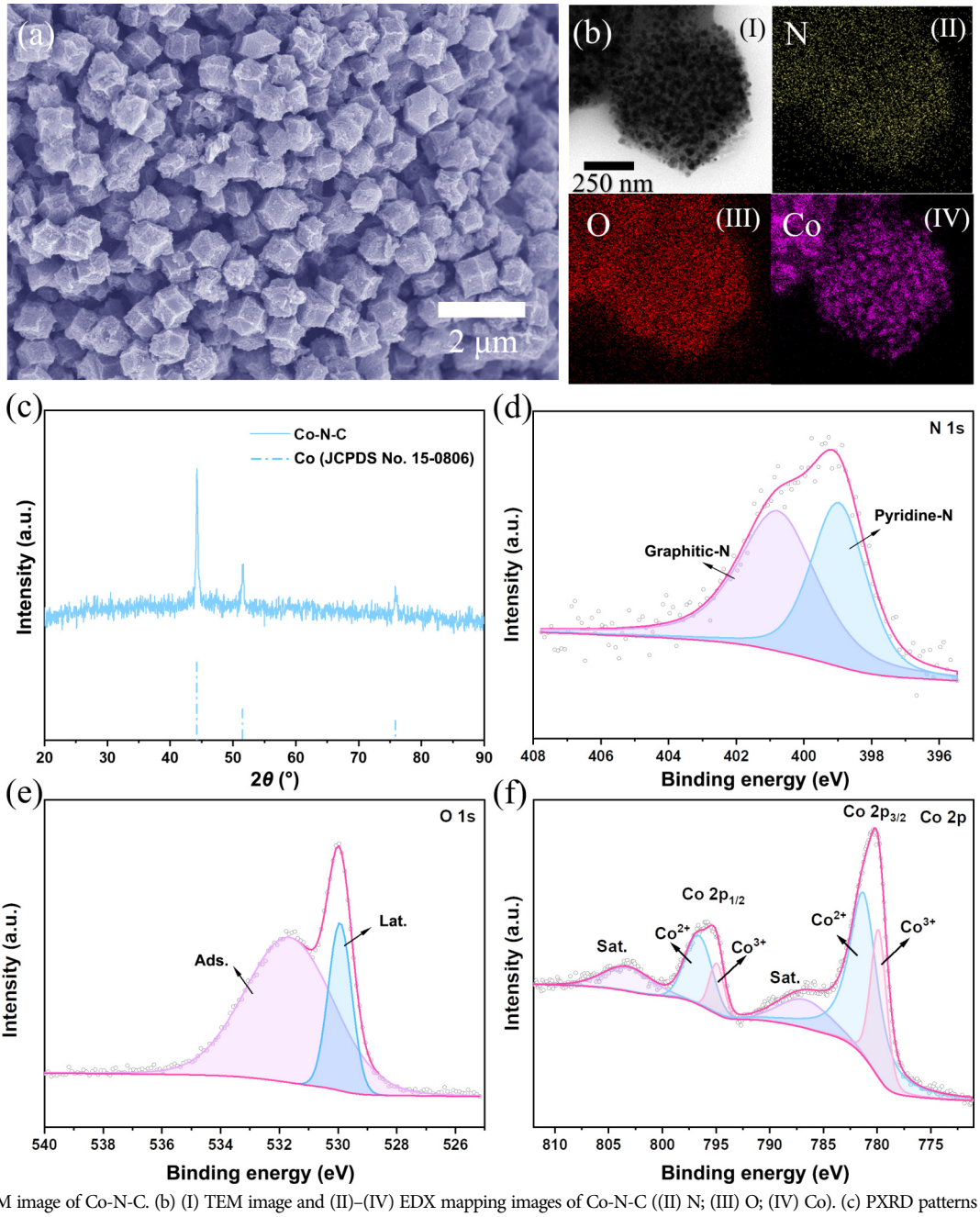

Figure 1 (a) SEM image of Co-N-C. (b) (I) TEM image and (II)–(IV) EDX mapping images of Co-N-C ((II) N; (III) O; (IV) Co). (c) PXRD patterns of Co-N-C. XPS spectra of Co-N-C ((d) N 1s; (e) O 1s; (f) Co 2p).

lattice oxygen [28] in the catalyst and oxygen adsorbed on the surface [29] (Fig. 1(e)). The main peak in the Co 2p spectrum is resolved into six peaks in Fig. 1(f), which consist of two shakeup satellites and four spin-orbit doublets. The binding energies at 781.28 and 796.60 eV can be assigned to Co^{2+} $2p_{3/2}$ and Co^{2+} $2p_{1/2}$ [30] with two satellite peaks of 786.73 and 803.25 eV [31]. The two peaks with lower binding energies of 779.86 and 794.94 eV can be assigned to Co^{3+} $2p_{3/2}$ and Co^{3+} $2p_{1/2}$ [32]. Minor surface oxidation of the Co nanoparticles may be the cause of just Co^{2+} and Co^{3+} existing but not Co^0 in the Co 2p spectrum of Co-N-C [33].

We evaluated the e NO_3^-RR performance of catalysts in an H-cell under environmental conditions. Unless otherwise noted, all reactions were performed in a 70 mL neutral electrolyte containing 0.05 M sodium sulfate (SO_4^{2-}) and 0.05 M sodium nitrate (NO_3^-). Figure 2(a) shows the LSV curves of the $Co(OH)_2$@Co-N-C with/without NO_3^-. On the electrode's surface, only hydrogen evolution takes place if the electrolyte contains only SO_4^{2-}. The initial potential of materials became significantly more negative after the addition of NO_3^- which proves the occurrence of nitrate reduction reaction. Meanwhile, a series of solutions containing different concentrations of NO_3^- are prepared as the reaction electrolyte. As is shown in Fig. 2(b), the current density increases obviously with the improvement of NO_3^- concentration. As the reaction moves forward, the amount of product increases simultaneously. Then, a 2-h *i–t* test at different voltages from −0.5 to −1.1 V (vs. RHE) was used to test the reactivity of $Co(OH)_2$@Co-N-C in the reduction reaction. The absorbance of NH_4^+ was measured using ultraviolet–visible spectrophotometry and the calibration curves were employed to determine the product concentrations. In the image Fig. 2(c), as the potential becomes more negative, the output of ammonia increases significantly, peaking at −1 V (vs. RHE) with an NH_3 yield of 2774.7 $\mu g \cdot h^{-1} \cdot cm^{-2}$ and an FE of 81.4%. On the contrary, the Faraday efficiency decreases as the potential increases (from 92.1% at −0.5 V (vs. RHE) to 62.3% at −1.1 V (vs. RHE)), mainly due to the intensification of the hydrogen evolution reaction. Meanwhile, the byproducts at different potentials were also measured. And we measured the concentration of N_2H_4 using the Watt–Chrisp method and no hydrazine production was detected at each potential. The concentration of NO_2^- was also measured by colorimetry and from the Fig. 2(d), it can be seen that a small amount of nitrite ions is produced after the potential increases to −0.9 V. Taking both factors into account, we choose −1 V (vs. RHE) as the best potential choice for the following electrochemistry test. Figure 2(e) shows the results without NO_3^- and the catalytic performance of bare carbon paper. We can observe that almost no product is produced if there is no NO_3^- in the solution. When the carbon cloth is used as the working electrode, a low rate of 343 $\mu g \cdot h^{-1} \cdot cm^{-2}$ with an FE of 22.6% is obtained which proves the carbon paper substrate plays only a minor role in the reaction. Cyclic stability is usually one of the evaluation indicators of catalysts and we performed 12 consecutive 2-h chronoamperometric tests.

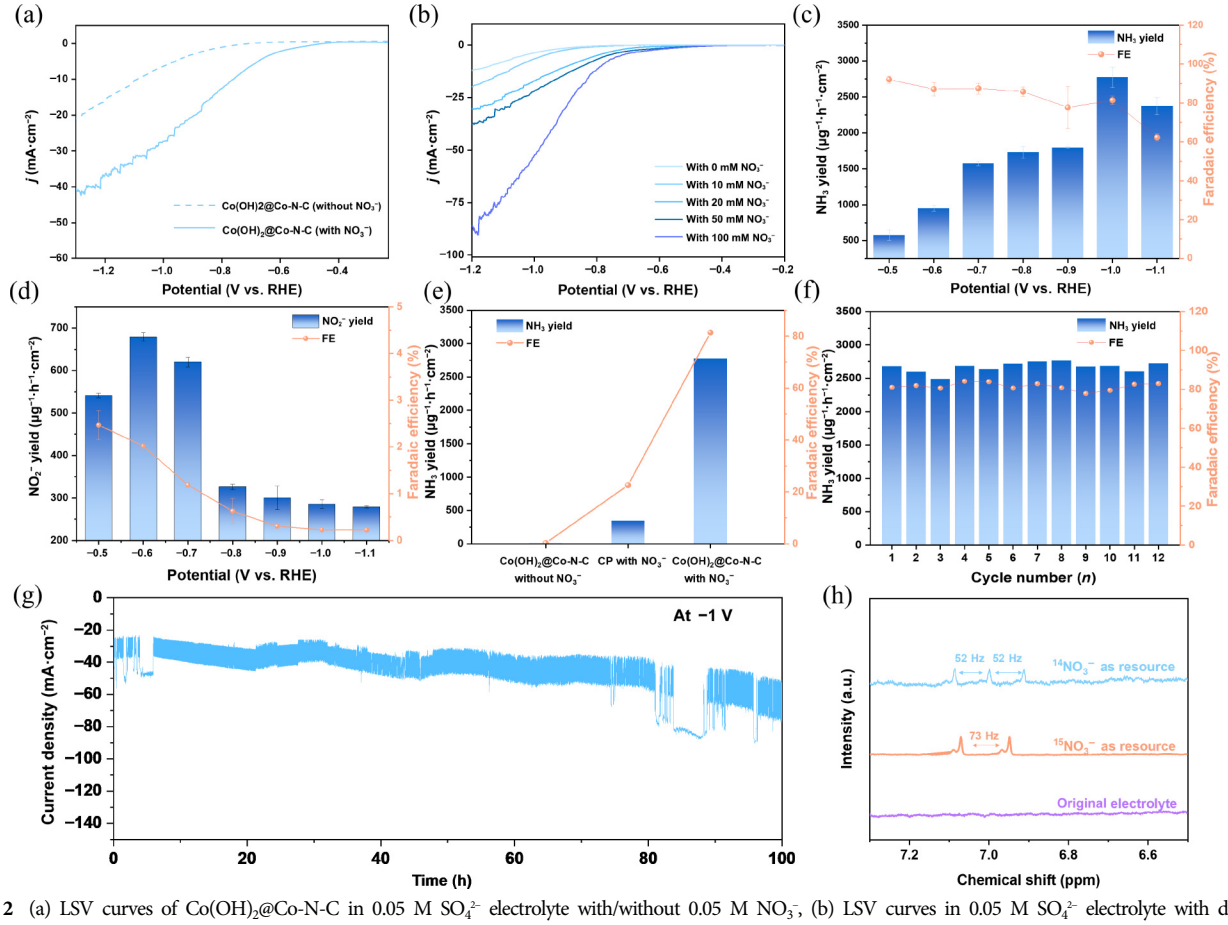

Figure 2 (a) LSV curves of $Co(OH)_2$@Co-N-C in 0.05 M SO_4^{2-} electrolyte with/without 0.05 M NO_3^-, (b) LSV curves in 0.05 M SO_4^{2-} electrolyte with different concentrations of NO_3^-, (c) potential-dependent NH_3 yield and Faradaic efficiency in 0.05 M SO_4^{2-} and 0.05 M NO_3^-, (d) potential-dependent NO_2^- yield and Faradaic efficiency, (e) NH_3 yield and Faradaic efficiency of CP and $Co(OH)_2$@Co-N-C, (f) the cycling tests of $Co(OH)_2$@Co-N-C at −1 V (vs. RHE), (g) the stability test for 100 h. (h) ^1H NMR spectra of the original electrolyte and electrolyte after 2 h of NO_3^-RR electrolysis using $^{14}NO_3^-$ and $^{15}NO_3^-$ as the nitrogen source.

As shown in Fig. 2(f), in the 12-round cycle test, there is no significant drop in both ammonia yield and FE, demonstrating that our material has good cycle stability in the reduction reaction. Meanwhile, we performed a 100-h chronoamperometric test using a flowing electrolyte and the reaction current density did not decrease during the 100 h also demonstrates the excellent stability of the $Co(OH)_2$@Co-N-C modified electrode (Fig. 2(g)). To exclude the possible nitrogen source effects, we conducted isotope experiments. Figure 2(h) shows the ^1H NMR spectrum of the original electrolyte, $^{14}NO_3^-$ as the reactant electrolyte and $^{15}NO_3^-$ as the reactant electrolyte. The ^1H NMR spectra of the original electrolyte is almost a straight line, proving that no ammonium is present. When using $^{14}NO_3^-$ as the feeding, there are three peaks on the spectrum with intervals of 52 Hz, while using $^{15}NO_3^-$ as the feeding results in only double peaks with intervals of 73 Hz [34]. This result is consistent with those documented in the literature, indicating that sodium nitrate—rather than ambient pollution—is the true source of the product ammonia.

After the chronoamperometry test, we characterized the morphology and crystal phase of the catalyst. Surprisingly, the shape of the catalyst changed from a regular dodecahedral structure to a nanosheet structure after the reaction (Fig. 3(a)). Figures 3(b) and 3(c) show the TEM and HRTEM images after the reaction, we simultaneous confirms the lattice planes of (100) plane attribute to $Co(OH)_2$ and (200),(111) planes attribute to metal Co. Figure 3(d) exhibit the dark field image and its correlation energy-dispersive X-ray (EDX) mapping images of the catalyst after reduction reaction which displays the C, N, Co, O elements uniformly distributed on the nanosheets. In order to further characterize the phase composition and valence state after the reaction, XRD and XPS measurements were applied. As shown in Fig. 4(a), the two diffraction peaks at 19.1° and 37.9° are attributed to the (001) plane and (101) plane of $Co(OH)_2$ [35] (JCPDS No. 30-0443). We can also observe three characteristic peaks that belong to metal Co which corresponds well to the result of HRTEM measurement. In the Co 2p spectra (Fig. 4(b)) of the two samples, we can observe that the characteristic peak of Co moved to the high-energy region after the reduction reaction. The two peaks located at 781.35 and 797.40 eV are attributed to Co^{2+} $2p_{3/2}$ and Co^{2+} $2p_{1/2}$, respectively. All the characterization results point to one conclusion: The interwoven nanosheets formed *in-situ* during the reaction are composed of the metal Co and $Co(OH)_2$ and we call it $Co(OH)_2$@Co-N-C.

To figure out the nature of catalyst morphology change and the dynamic evolution of Co species in the as-prepared $Co(OH)_2$@Co-N-C catalyst and a series of experiments were set up to characterize this process. Firstly, we evenness sprayed the material onto a piece of carbon paper and immersed it in a 0.05 M NO_3^- and 0.05 M SO_4^{2-} mixed solution. Then we took the samples from solution every 10 min, diluted them and measured the UV spectra to detect the NO_2^- concentration in the solution. As shown in Fig. 5(a), the NO_2^- concentration in the solution gradually increases with time, reached 0.137 ppm after 50 min. The NO_2^- is produced even without an external voltage applied, this demonstrates a spontaneous redox reaction between the Co^0 in the Co-N-C and the NO_3^- in the electrolyte. At this point, the concentration of leached Co^{2+} in the solution from the Co nanoparticles encapsulated in the C shell of Co-N-C was measured using the inductively coupled plasma (ICP) method. The ICP method result displays Co^{2+} concentration in electrolyte this moment was 0.24 $mg{\cdot}L^{-1}$ proving that the C-encapsulated Co^0 leached into the solution during the spontaneous redox reaction. When NO_3^- converts to NO_2^-, metal Co in Co-N-C is converted to Co^{2+}. The SEM image after 24 h of immersion was demonstrated in Fig. 5(b). We can observe that after the spontaneous reaction, the morphology remains consistent with the primary sample. At this point, Co-N-C does not transform into an interwoven aggregate nanosheet structure, which proves that the influence of current is also an essential reason for the

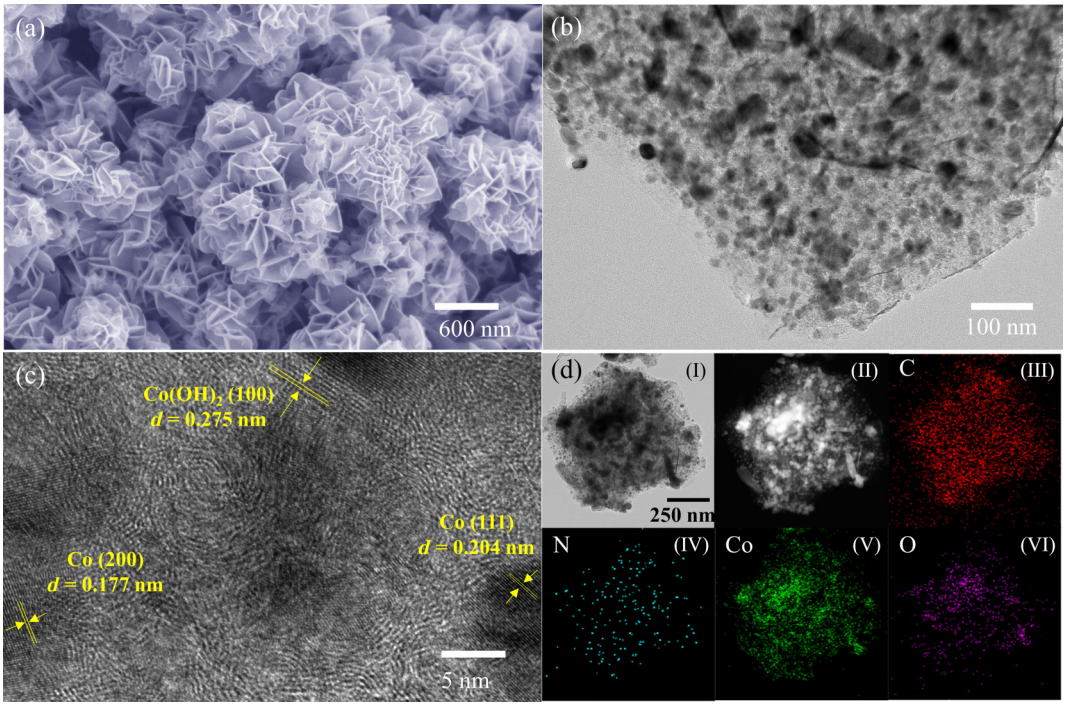

Figure 3 (a) SEM image, (b) TEM image, and (c) HRTEM image of $Co(OH)_2$@Co-N-C. (d) (I) TEM image, (II) dark field image, and (III)–(VI) EDX mapping images of the catalyst after reaction ((III) C; (IV) N; (V) Co; (VI) O).

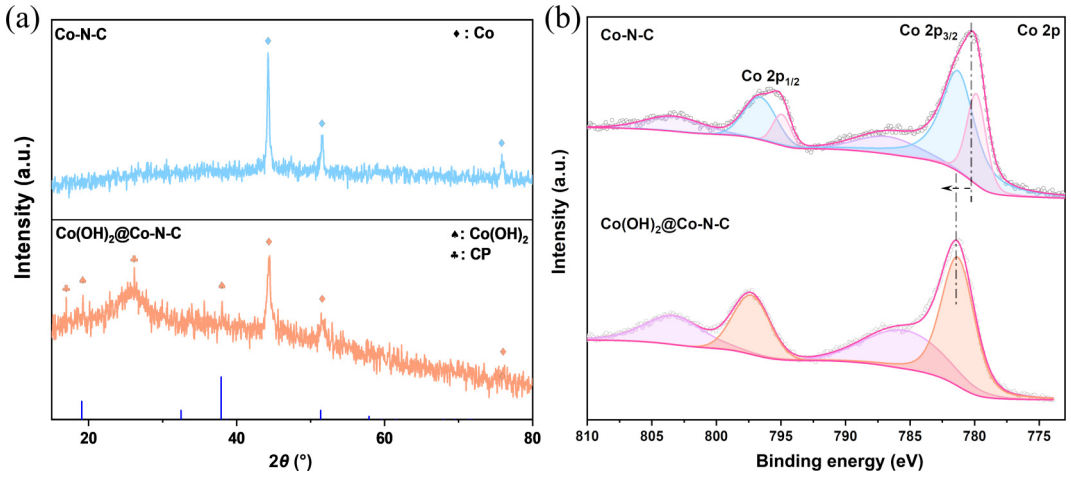

Figure 4 (a) XRD patterns and (b) Co 2p spectrums of the catalyst before and after the reaction.

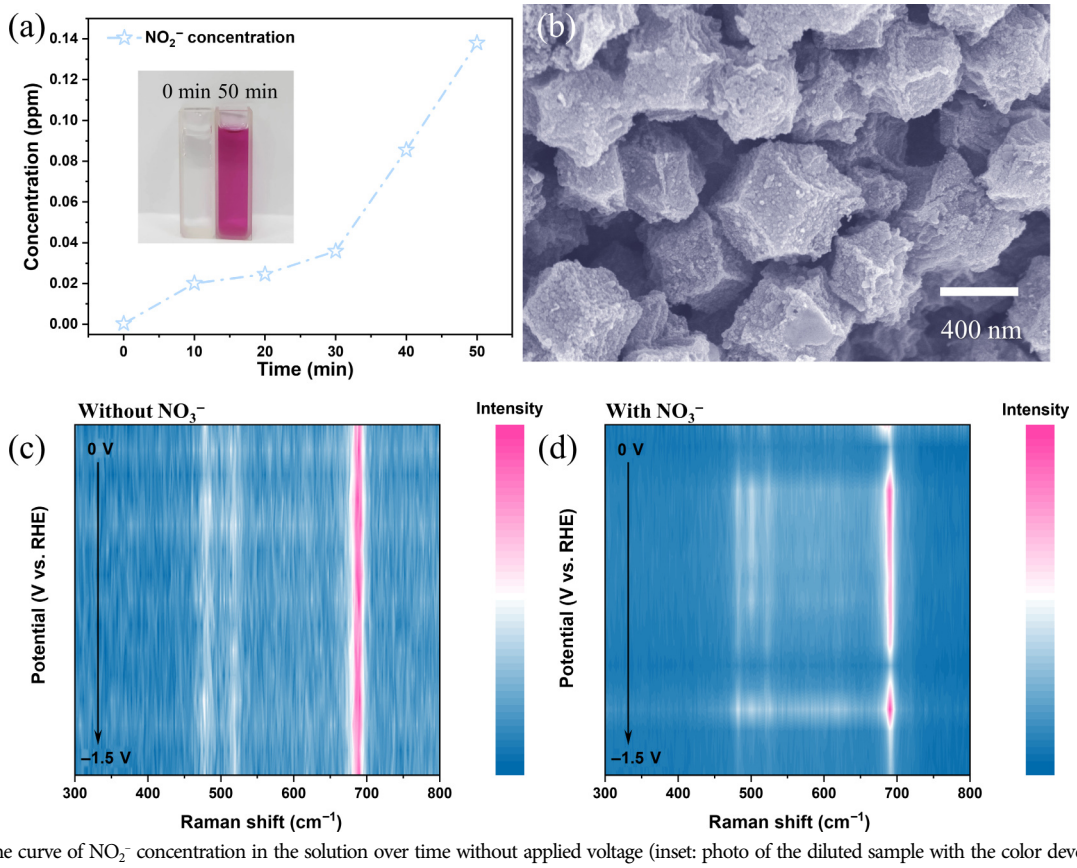

Figure 5 (a) The curve of NO_2^- concentration in the solution over time without applied voltage (inset: photo of the diluted sample with the color developer). (b) SEM image of Co-N-C after immersion for 24 h without voltage applied. (c) *In-situ* Raman spectroscopy of $Co(OH)_2$@Co-N-C from 0 to −1.5 V (vs. RHE) without NO_3^-. (d) *in-situ* Raman spectroscopy of $Co(OH)_2$@Co-N-C from 0 to −1.5 V (vs. RHE) with NO_3^-.

change in morphology. And Fig. S3 in the ESM is the XRD pattern of the sample after immersion for 24 h. As is shown in the picture, the sharp peak at 18.1° and the broad peak at 25.7° are attributed to the characteristic peak of carbon paper. The relative strength of the three peaks at 44.2°, 51.5° and 75.9°, which are assigned to Co^0 has decreased clearly (Fig. S4 in the ESM), proving the conversion of Co^0 to Co^{2+}. However, the diffraction peak intensity of the $Co(OH)_2$@Co-N-C after the eNO_3^-RR is back to strength (Fig. S4 in the ESM), this proves that under the action of electric reduction, Co^{2+} in $Co(OH)_2$ reverts to Co^0. Subsequently, the newly formed Co^0 will participate in another reaction cycle. The concentration of Co^{2+} in the solution after a 2-h reduction reaction was also measured by the ICP method, with just 4 μg·L^{-1}. Compared to the Co^{2+} concentration without applied voltage, there's almost no Co^{2+} in the solution after the reduction reaction. This proves that the dissolved Co^{2+} in the electrolyte has comprehensively transformed into $Co(OH)_2$. To further verify the transform mechanism of the valence states during the cycling, *in-situ* electrochemical Raman tests were carried out. Figures 5(c) and 5(d) demonstrate the Raman spectroscopy of $Co(OH)_2$@Co-N-C from 0 to −1.5 V (vs. RHE) in electrolytes without and with NO_3^-. The three characteristic peaks at 474, 512 and 680 cm^{-1} correspond to the E_g,

F_{2g} and A_1 modes in Co nanoparticles [36]. In the absence of NO_3^-, the characteristic peak intensity of Co nanoparticles did not change significantly. However, in the electrolyte containing nitrate ions, characteristic peaks of Co disappear and reappear in a continuous cycle. All of the above tests, taken together, support our proposed mechanism for the redox cycling of the Co valence state and the reasons for the morphological changes.

The reaction mechanism of eNO_3^-RR on Co-N-C we deduced can be described by Scheme 2 and explained as follows: spontaneous reaction between Co nanoparticles and NO_3^- results in the formation of Co^{2+} and NO_2^-. The combination of Co^{2+} and OH^- from the electrolysis of water ($H_2O \rightarrow H^+ + OH^-$) led to the formation of $Co(OH)_2$. In addition, the constant transfer of electrons from the cathode also causes Co^{2+} to be converted to Co^0, creating a dynamic cycle of Co species. The occurrence of spontaneous reaction can effectively solve the high energy barrier of adsorption and activation of NO_3^- and improve the reduction reaction performance of catalysts. At the same time, the regular dodecahedron structure of Co-N-C turns into interwoven nanosheets like $Co(OH)_2$@Co-N-C due to the combined by partially dissolved Co^{2+} and OH^- in the electrolyte. On the other hand, NO_2^- is further reduced by electrocatalysis, continuously protonated (H^+ from Volmer step) and finally converted to ammonia.

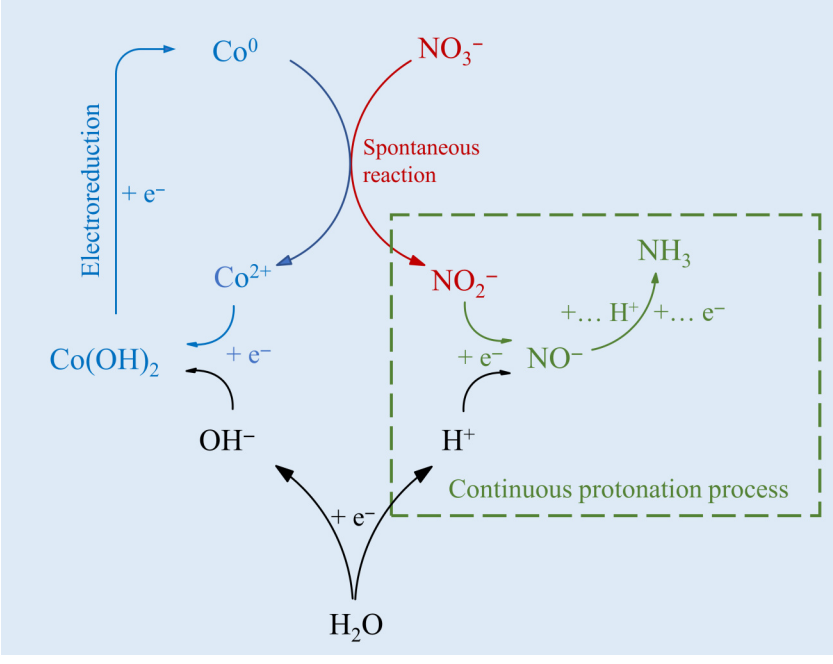

Scheme 2 The potential mechanism of the eNO_3^-RR on Co-N-C and dynamic evolution of Co species.

In addition, the performance of Co-N-C in the electrochemical nitrogen reduction reaction (eNRR) has also been tested in 0.1 M KOH with saturated nitrogen in an H-cell for 2 h. As shown in Fig. 6(a), the NH_3 yield-dependent potential trend first increases, then decreases, reaching a maximum of 20.9 $\mu g \cdot h^{-1} \cdot cm^{-2}$ with an FE of 6.91% at −0.4 V (vs. RHE). After 8 cycles of 2 h each, the NH_3 yield and FE were still over 90% of the first test, confirming the outstanding stability of our catalyst in NRR (Fig. 6(b)). Furthermore, we tested the cyclic voltammetry (CV) curve at different scan rates from 50 to 100 $mV \cdot s^{-1}$ in deionized water (Fig. 6(c)). The electrochemical active surface area (ECSA) of Co-N-C is obtained for 4.77 $mF \cdot cm^{-2}$ (Fig. 6(d)). In conclusion, the as-prepared Co-N-C is expected to be a bifunctional catalyst for electrocatalytic ammonia production.

4 Conclusion

To sum up, the Co-N-C derived from ZIF-67 has an excellent performance in converting NO_3^- into ammonia. We achieve an NH3 yield of 2774.7 $\mu g \cdot h^{-1} \cdot cm^{-2}$ with a FE of 81.4% at −1 V (vs. RHE) in neutral solution which is superior to most reported catalysts. During the reaction process, the valence of Co species was continuously transformed between Co^0 and Co^{2+}. The spontaneous reaction between Co nanoparticles and NO_3^- in electrolyte, successfully solved the energy loss caused by the high adsorption and activation energy barrier of NO_3^-. In addition, the reconstruction of morphology brings a larger specific surface area, exposing more Co-sites on the surface of the interwoven nanosheet, which effectively improves the catalytic performance and stability of the catalyst. Our work explores the reasons for the morphological changes and valence state dynamics of the Co-species before and after the reaction and provides more ideas at the design level for the application of Co-based catalysts in electrochemical nitrate reduction in neutral solution.

Electronic Supplementary Material: Supplementary material (ion concentration detection methods and other material characterizations) is available in the online version of this article at https://doi.org/10.26599/NR.2025.94907038.

Data availability

All data needed to support the conclusions in the paper are presented in the manuscript and the Electronic Supplementary Material. Additional data related to this paper may be requested from the corresponding author upon request.

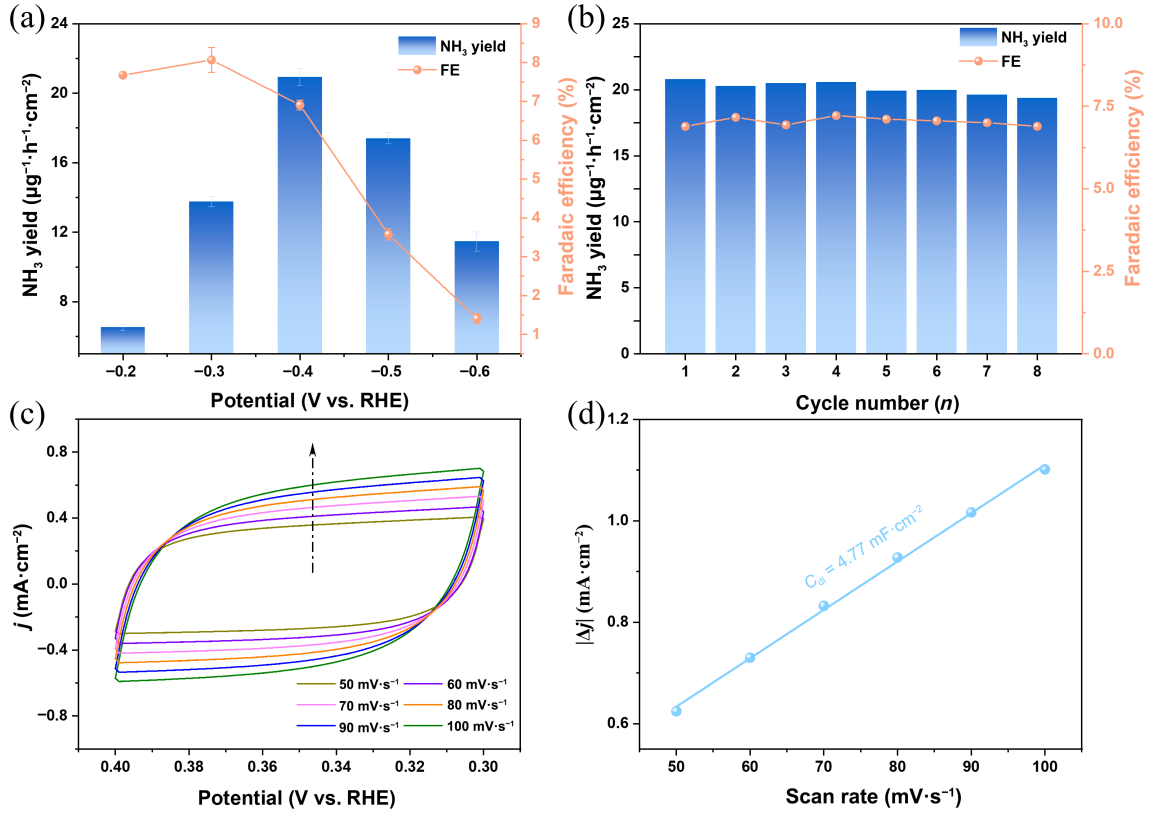

Figure 6 (a) Potential-dependent NH_3 yield and Faradaic efficiency of Co-N-C in NRR test. (b) cyclic stability test of Co-N-C in NRR test. (c) CV curves of the Co-N-C with various scan rates from 50 to 100 mV·s^{-1}. (d) the ECSA of the Co-N-C.

Acknowledgements

This work was financially supported by the National Natural Science Foundation of China (No. 22175030) and the Open Project of State Key Laboratory of Supramolecular Structure and Materials (No. sklssm 202406). Special thanks are due to the instrument from the Analytical and Testing Center, Northeastern University.

Declaration of competing interest

All the contributing authors report no conflict of interests in this work.

Author contribution statement

Y. L. F.: Data curation, validation, writing manuscript, experimental design. X. T. Y. and Y. Y.: Visualization. K. Z., X. Y. Y., and A. X. Z.: Software. X. J. H., B. B. C., and Y. H. L.: Investigation. F. Q. F.: Review. Y. F.: Supervision, project administration. All the authors have approved the final manuscript.

Use of AI statement

None.

References

[1] Van Langevelde, P. H.; Katsounaros, I.; Koper, M. T. M. Electrocatalytic nitrate reduction for sustainable ammonia production. *Joule* **2021**, *5*, 290–294.

[2] Chen, J. G.; Crooks, R. M.; Seefeldt, L. C.; Bren, K. L.; Bullock, R. M.; Darensbourg, M. Y.; Holland, P. L.; Hoffman, B.; Janik, M. J.; Jones, A. K. et al. Beyond fossil fuel-driven nitrogen transformations. *Science* **2018**, *360*, eaar6611.

[3] Lehnert, N.; Musselman, B. W.; Seefeldt, L. C. Grand challenges in the nitrogen cycle. *Chem. Soc. Rev.* **2021**, *50*, 3640–3646.

[4] Ritchie, S. M. C.; Bhattacharyya, D. Membrane-based hybrid processes for high water recovery and selective inorganic pollutant separation. *J. Hazard. Mater.* **2002**, *92*, 21–32.

[5] Samatya, S.; Kabay, N.; Yüksel, Ü.; Arda, M.; Yüksel, M. Removal of nitrate from aqueous solution by nitrate selective ion exchange resins. *React. Funct. Polym.* **2006**, *66*, 1206–1214.

[6] Yang, G. C. C.; Lee, H. L. Chemical reduction of nitrate by nanosized iron: Kinetics and pathways. *Water Res.* **2005**, *39*, 884–894.

[7] Gao, J. N.; Jiang, B.; Ni, C. C.; Qi, Y. F.; Zhang, Y. Q.; Oturan, N.; Oturan, M. A. Non-precious Co_3O_4–TiO_2/Ti cathode based electrocatalytic nitrate reduction: Preparation, performance and mechanism. *Appl. Catal., B: Environ.* **2019**, *254*, 391–402.

[8] Gao, Y. H.; Wang, K. P.; Li, S. K.; Zhang, H.; Huang, F. Z. Enhancing the selective electrochemical conversion of nitrate via π back-donation on Lewis acid sites induced by noble-metal doped CoP. *J. Mater. Chem. A* **2023**, *11*, 21161–21169.

[9] Chen, F. Y.; Wu, Z. Y.; Gupta, S.; Rivera, D. J.; Lambeets, S. V.; Pecaut, S.; Kim, J. Y. T.; Zhu, P.; Finfrock, Y. Z.; Meira, D. M. et al. Efficient conversion of low-concentration nitrate sources into ammonia on a Ru-dispersed Cu nanowire electrocatalyst. *Nat. Nanotechnol.* **2022**, *17*, 759–767.

[10] Wu, Z. Y.; Karamad, M.; Yong, X.; Huang, Q. Z.; Cullen, D. A.; Zhu, P.; Xia, C.; Xiao, Q. F.; Shakouri, M.; Chen, F. Y. et al. Electrochemical ammonia synthesis via nitrate reduction on Fe single atom catalyst. *Nat. Commun.* **2021**, *12*, 2870.

[11] Zhang, S.; Li, M.; Li, J. C.; Song, Q. N.; Liu, X. High-ammonia selective metal-organic framework-derived Co-doped Fe/Fe_2O_3

catalysts for electrochemical nitrate reduction. *Proc. Natl. Acad. Sci. USA* **2022**, *119*, e2115504119.

[12] Wang, J. L.; Zhang, S. B.; Wang, C. C.; Li, K.; Zha, Y. K.; Liu, M.; Zhang, H. M.; Shi, T. F. Ambient ammonia production via electrocatalytic nitrate reduction catalyzed by a flower-like $CuCo_2O_4$ electrocatalyst. *Inorg. Chem. Front.* **2022**, *9*, 2374–2378.

[13] Yang, J.; Qi, H. F.; Li, A. Q.; Liu, X. Y.; Yang, X. F.; Zhang, S. X.; Zhao, Q.; Jiang, Q. K.; Su, Y.; Zhang, L. L. et al. Potential-driven restructuring of Cu single atoms to nanoparticles for boosting the electrochemical reduction of nitrate to Ammonia. *J. Am. Chem. Soc.* **2022**, *144*, 12062–12071.

[14] Zhou, J.; Wen, M.; Huang, R.; Wu, Q. S.; Luo, Y. X.; Tian, Y. K.; Wei, G. F.; Fu, Y. Q. Regulating active hydrogen adsorbed on grain boundary defects of nano-nickel for boosting ammonia electrosynthesis from nitrate. *Energy Environ. Sci.* **2023**, *16*, 2611–2620.

[15] Liu, Y. T.; Qiu, W. X.; Wang, P. F.; Li, R.; Liu, K.; Omer, K. M.; Jin, Z. Y.; Li, P. P. Pyridine-N-rich Cu single-atom catalyst boosts nitrate electroreduction to ammonia. *Appl. Catal. B: Environ.* **2024**, *340*, 123228.

[16] Li, H. M.; Li, S. P.; Guan, R. J.; Jin, Z. Y.; Xiao, D.; Guo, Y.; Li, P. P. Modulating the surface concentration and lifetime of active hydrogen in Cu-based layered double hydroxides for electrocatalytic nitrate reduction to ammonia. *ACS Catal.* **2024**, *14*, 12042–12050.

[17] Li, H. M.; Li, P. P.; Guo, Y.; Jin, Z. Y. Electrochemical probing the site reactivity in iron single-atom catalysts for electrocatalytic nitrate reduction to ammonia. *Anal. Chem.* **2024**, *96*, 997–1002.

[18] Li, R.; Gao, T. T.; Qiu, W. X.; Xie, M. H.; Jin, Z. Y.; Li, P. P. Unveiling the size effect of nitrogen-doped carbon-supported copper-based catalysts on nitrate-to-ammonia electroreduction. *Nano Res.* **2024**, *17*, 2438–2443.

[19] Liu, K.; Li, H. M.; Xie, M. H.; Wang, P. F.; Jin, Z. Y.; Liu, Y. T.; Zhou, M.; Li, P. P.; Yu, G. H. Thermally enhanced relay electrocatalysis of nitrate-to-ammonia reduction over single-atom-alloy oxides. *J. Am. Chem. Soc.* **2024**, *146*, 7779–7790.

[20] Li, P. P.; Liao, L.; Fang, Z. W.; Su, G. H.; Jin, Z. Y.; Yu, G. H. A multifunctional copper single-atom electrocatalyst aerogel for smart sensing and producing ammonia from nitrate. *Proc. Natl. Acad. Sci. USA* **2023**, *120*, e2305489120.

[21] Wang, J.; Cai, C.; Wang, Y. A.; Yang, X. M.; Wu, D. J.; Zhu, Y. M.; Li, M. H.; Gu, M.; Shao, M. H. Electrocatalytic reduction of nitrate to ammonia on low-cost ultrathin CoO_x nanosheets. *ACS Catal.* **2021**, *11*, 15135–15140.

[22] Yang, J. Y.; Zhang, W. D.; Zhao, H.; Zou, Y. Z.; Zhang, Z. Y.; Liu, J. Y.; Wang, J.; Gu, Z. G.; Yan, X. D. High-valent cobalt active sites derived from electrochemical activation of metal-organic frameworks for efficient nitrate reduction to ammonia. *Appl. Catal., B: Environ.* **2024**, *340*, 123237.

[23] Han, S. H.; Li, H. J.; Li, T. L.; Chen, F. P.; Yang, R.; Yu, Y. F.; Zhang, B. Ultralow overpotential nitrate reduction to ammonia via a three-step relay mechanism. *Nat. Cat.* **2023**, *6*, 402–414.

[24] Liang, S. Z.; Teng, X.; Xu, H.; Chen, L. S.; Shi, J. L. H* species regulation by Mn-$Co(OH)_2$ for efficient nitrate electro-reduction in neutral solution. *Angew. Chem., Int. Ed.* **2024**, *63*, e202400206.

[25] Liu, H. F.; Qin, J. Z.; Mu, J. C.; Liu, B. J. *In situ* interface engineered Co/NC derived from ZIF-67 as an efficient electrocatalyst for nitrate reduction to ammonia. *J. Colloid Interface Sci.* **2023**, *636*, 134–140

[26] Chen, X. L.; Zhang, G. W.; Shi, L.; Pan, S. Q.; Liu, W.; Pan, H. Au/ZnO hybrid nanocatalysts impregnated in N-doped graphene for simultaneous determination of ascorbic acid, acetaminophen and dopamine. *Mater. Sci. Eng.: C* **2016**, *65*, 80–89.

[27] Wang, Z. J.; Li, B.; Ge, X. M.; Goh, F. W. T.; Zhang, X.; Du, G. J.; Wuu, D.; Liu, Z. L.; Andy Hor, T. S.; Zhang, H. et al. Co@Co_3O_4@PPD core@bishell nanoparticle-based composite as an efficient electrocatalyst for oxygen reduction reaction. *Small* **2016**, *12*, 2580–2587.

[28] Yu, Z. Q.; Sun, T. Y.; Liu, B. S.; Zhang, L.; Chen, H. J.; Fan, X. S.; Sun, Z. J. Self-rectifying and forming-free nonvolatile memory behavior in single-crystal TiO_2 nanowire memory device. *J. Alloys Compd.* **2021**, *858*, 157749.

[29] Zheng, W.; Lu, X. F.; Wang, W.; Li, Z. Y.; Zhang, H. N.; Wang, Y.; Wang, Z. J.; Wang, C. A highly sensitive and fast-responding sensor based on electrospun In_2O_3 nanofibers. *Sens. Actuators B: Chem.* **2009**, *142*, 61–65.

[30] Wang, P.; Wang, S.; Zhang, X. M.; Wang, H. Q.; Duan, W.; Han, H. L.; Fan, X. L. Rational construction of CoO/CoF_2 coating on burnt-pot inspired 2D CNs as the battery-like electrode for supercapacitors. *J. Alloys Compd.* **2020**, *819*, 153374.

[31] Qin, Y. N.; Sun, Y. J.; Li, Y. J.; Li, C. J.; Wang, L.; Guo, S. J. MOF derived Co_3O_4/N-doped carbon nanotubes hybrids as efficient catalysts for sensitive detection of H_2O_2 and glucose. *Chin. Chem. Lett.* **2020**, *31*, 774–778.

[32] Yuan, H. F.; Wang, S. M.; Ma, Z. Z.; Kundu, M.; Tang, B.; Li, J. P.; Wang, X. G. Oxygen vacancies engineered self-supported B doped Co_3O_4 nanowires as an efficient multifunctional catalyst for electrochemical water splitting and hydrolysis of sodium borohydride. *Chem. Eng. J.* **2021**, *404*, 126474.

[33] Zhou, A. W.; Guo, R. M.; Zhou, J.; Dou, Y. B.; Chen, Y.; Li, J. R. Pd@ZIF-67 derived recyclable Pd-based catalysts with hierarchical pores for high-performance heck reaction. *ACS Sustain. Chem. Eng.* **2018**, *6*, 2103–2111.

[34] Zhang, R.; Guo, Y.; Zhang, S. C.; Chen, D.; Zhao, Y. W.; Huang, Z. D.; Ma, L. T.; Li, P.; Yang, Q.; Liang, G. J. et al. Efficient ammonia electrosynthesis and energy conversion through a Zn-nitrate battery by iron doping engineered nickel phosphide catalyst. *Adv. Energy Mater.* **2022**, *12*, 2103872.

[35] Wan, S. H.; Qi, J.; Zhang, W.; Wang, W. N.; Zhang, S. K.; Liu, K. Q.; Zheng, H. Q.; Sun, J. L.; Wang, S. Y.; Cao, R. Hierarchical Co(OH)F superstructure built by low-dimensional substructures for electrocatalytic water oxidation. *Adv. Mater.* **2017**, *29*, 1700286.

[36] Rauwel, E.; Al-Arag, S.; Salehi, H.; Amorim, C. O.; Cuisinier, F.; Guha, M.; Rosario, M. S.; Rauwel, P. Assessing cobalt metal nanoparticles uptake by cancer cells using live Raman spectroscopy. *Int. J. Nanomed.* **2020**, *15*, 7051–7062.